




# X-ray line profile analysis study on the evolution of the microstructure in additively manufactured 316L steel during severe plastic deformation

Jenő Gubicza<sup>1,\*</sup> , Megumi Kawasaki<sup>2</sup>, Zoltán Dankházi<sup>1</sup>, Márk Windisch<sup>1,3</sup>, and Moustafa El-Tahawy<sup>1,4</sup>

<sup>1</sup> Department of Materials Physics, Eötvös Loránd University, Budapest, P.O.B. 32, 1518, Hungary

<sup>2</sup> School of Mechanical, Industrial and Manufacturing Engineering, Oregon State University, Corvallis, OR 97331, USA

<sup>3</sup> Department of Development, Bay Zoltán Nonprofit Ltd. for Applied Research, Budapest 1116, Hungary

<sup>4</sup> Physics Department, Faculty of Science, Tanta University, Tanta 31527, Egypt

Received: 5 September 2023

Accepted: 8 October 2023

© The Author(s), 2023

## ABSTRACT

316L stainless steel was manufactured by additive manufacturing (AM), and then, the samples were severely deformed by the high-pressure torsion (HPT) technique. The evolution of the microstructure was monitored by X-ray line profile analysis. This method gives the crystallite size and the density of lattice defects, such as dislocations and twin faults. The AM-processing of the HPT disks was performed in two different modes: the laser beam was parallel or orthogonal to the normal direction of the disks. The subsequent HPT deformation was carried out for ½, 1, 5 and 10 turns. The microstructure and hardness evolution during HPT were similar regardless of the laser beam direction. For both sample series, the minimum achievable crystallite size was about 30 nm, while the dislocation density and the twin fault probability got saturated at the values of  $300\text{--}350 \times 10^{14} \text{ m}^{-2}$  and 3.5–4%, respectively. The microstructure evolution during HPT of the AM-prepared 316L steel was compared with the HPT-induced changes in an as-cast counterpart. It was found that while the AM-prepared 316L steel remained a single-phase face-centered cubic  $\gamma$ -structure during HPT, in the as-cast samples a body-centered cubic (bcc) martensitic  $\alpha$ -phase became the main phase with increasing the imposed strain of HPT due to the lower Ni content. In the saturation state achieved by HPT the initially as-cast 316L steel had a considerably higher hardness (about 6000 MPa) than that for the AM-prepared samples (~ 5000 MPa) due to the large fraction of the hard bcc phase formed during HPT.

Handling Editor: M. Grant Norton.

Address correspondence to E-mail: jeno.gubicza@ttk.elte.hu

<https://doi.org/10.1007/s10853-023-09030-0>

Published online: 30 October 2023

## Introduction

Materials in the stainless-steel family usually contain a high fraction of Cr (17–19 wt%) and Ni (9–12 wt%) since the former and latter elements hinder corrosion in air- and chloride-containing human body fluids, respectively [1–5]. 316L steel is one of the most frequently used members of the stainless-steel family, which is often applied as an orthopedic implant and structural material in nuclear power plants [4–7]. The specialty of the composition of this alloy is the relatively high amount of Mo (about 2 wt%) and a low concentration of carbon (<0.03 wt%), which also improves the corrosion resistance [2]. The low carbon content is indicated by the letter L in the name of the alloy. Besides the increase of the corrosion resistance, Ni addition has another role: it stabilizes the metastable face-centered cubic (fcc) austenite structure at room temperature (RT) even during plastic deformation, which yields a good ductility of 316L steel [6, 8]. Thus, the elongation to failure can reach 84% in room-temperature tensile testing [9]. With decreasing Ni content in stainless steels, a phase transformation from austenite to martensite can occur during deformation, which contributes to the strength enhancement besides strain hardening since the martensite phase has a hard body-centered (bcc) structure [10, 11]. Due to the combination of elevated strength, good ductility, high fracture toughness, excellent corrosion resistance and low absorption rate of neutron radiation, 316L can serve as a structural material in nuclear power plants [12].

Additive manufacturing (AM) or 3D-printing of metallic materials is an emerging technology that can provide three-dimensional parts directly in their final shape; therefore, additional machining is not required, resulting in a minimization of waste material during processing [13]. In most AM methods, the samples are built layer by layer using a computer-controlled laser beam melting of powder particles [14]. After 3D-printing of metallic components, very often post-processing sintering (e.g., by applying hot isostatic pressing [15]) and annealing [16] are applied for reducing the remaining porosity and releasing the residual stresses, respectively. AM-processing has also been used for the production of parts from 316L steel [17–21]. The residual stresses [22, 23] the microstructure including porosity [24–31], the mechanical performance [22, 25, 32–46] and the corrosion properties [47–59] of AM-prepared 316L samples have been extensively studied.

Concerning the mechanical behavior, uniaxial loading [39, 46], fatigue tests [34, 37, 41] and tribology measurements [40, 44] were performed. For instance, the effect of the relative orientation between the loading axis and the building direction on the tensile performance has been revealed [46].

The mechanical performance of metallic materials at very high strains can be studied using severe plastic deformation (SPD) techniques [60]. These methods apply high hydrostatic stress to suppress cracking during deformation, thereby achieving extremely large strains without failure of the specimen [61]. The highest imposed strain can be achieved by high-pressure torsion (HPT) technique: the maximum shear strain is usually about 400 or higher at the edge of the HPT-processed disks processed for large numbers of turns [62–64]. Therefore, in strongly alloyed metals, such as 316L steel, nanocrystallization of the microstructure also occurs during HPT performed at RT [65]. HPT processing has also been carried out on 3D-printed 316L stainless steel in order to study the microstructure evolution at extremely high strains [66]. It was found that after 8 turns of HPT the average grain size was refined to ~60 nm and the grains contained numerous twin boundaries with the spacing of few nanometers. After HPT, the material remained mainly fcc with a marginal fraction of  $\epsilon$ -martensite having a hexagonal close-packed (hcp) structure. Although the dislocation density was also tried to determine from the peak breadth, the applied Williamson–Hall method is not suitable to obtain a reliable value of the density of dislocations since only the evaluation of the full XRD line profile is able to give this quantity [67–69]. Additionally, due to the low stacking fault energy (SFE) of the fcc structure of 316L steel the high amount of deformation twins formed during HPT also causes peak broadening, which was not considered in the applied Williamson–Hall evaluation procedure. Thus, a reliable characterization of the evolution of the lattice defect density in AM-prepared 316L steel samples during HPT deformation is missing from the literature.

In this study, the effect of severe plastic deformation (SPD) on the microstructure of 3D-printed 316L stainless-steel samples was investigated. SPD-processing was performed by high-pressure torsion (HPT) technique, which imposes a superior strain on metallic materials compared to other SPD methods. The application of HPT on alloys usually results in the formation of a nanocrystalline microstructure with an

extremely large lattice defect density [65, 70]. A reliable characterization of severely deformed nanostructures can be carried out by X-ray line profile analysis (XLPA). This technique can describe the density of defects, such as dislocations and twin faults, with better statistics than the microscopy methods due to the orders of magnitude larger probed volume [68]. Other important advantages of XLPA are the non-destructivity and easy sample preparation. In the present investigation, AM-processing before HPT was carried out in two ways: the building direction during 3D-printing was either parallel or orthogonal to the normal vector of the HPT disk surface. The average crystallite size, the dislocation density and the twin fault probability were determined by XLPA for different numbers of HPT turns and analyzed as a function of the imposed shear strain. The results are compared with the microstructure evolution in another 316L steel, which was first cast and then processed by HPT under the same conditions. This work was motivated by the fact that a reliable characterization of the evolution of the lattice defect density in AM-processed 316L steel at high plastic strains is missing from the literature, although this material is of a great practical importance. The knowledge of the evolution of the defect structure can help revealing the deformation mechanisms and understanding the mechanical behavior of AM-processed 316L steel at high strains. Since the lattice defect evolution during SPD may be influenced by the direction of 3D-printing, the study of this effect has also a great significance.

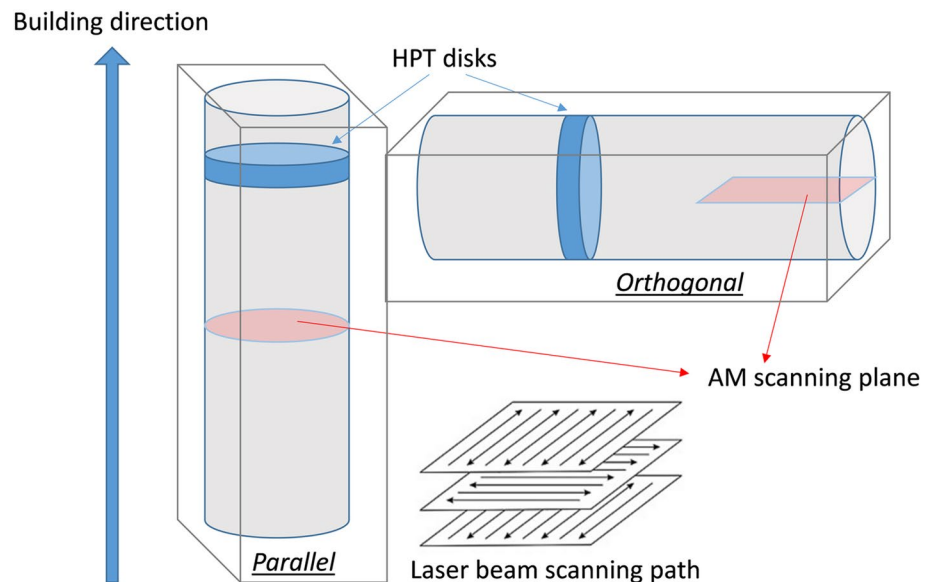
## Materials and methods

### Processing of the samples

The samples were fabricated using Höganäs AM 316L stainless-steel powder with particle sizes ranging from 20 to 53  $\mu\text{m}$ . The TruPrint 1000 (TRUMPF) metal 3D printer was employed for the manufacturing process. Printing parameters were selected in line with the manufacturer recommendations for 316 stainless steel. This includes a laser power of 113 W, laser speed of 700 mm/s, 20  $\mu\text{m}$  layer thickness, 55  $\mu\text{m}$  laser spot diameter, and an 80  $\mu\text{m}$  hatch spacing. These AM-processing parameters resulted in an approximate laser energy density of 161  $\text{J}/\text{mm}^3$  [24]. The printing process used sequential line scanning with a 90° rotation of the scan vector between successive layers. The printing process was carried out under an argon (Ar) atmosphere with a gas velocity of 2.5 m/s, maintaining the oxygen concentration in the chamber below 0.3 at. %.

The cylindrical billets processed by AM were sliced by electric discharge machining (EDM) into disks with a thickness of  $\sim 0.85$  mm and a diameter of about 10 mm. Figure 1 shows schematically the relative orientation between the laser beam (or printing) direction of AM-processing and the disks cut for HPT. As can be seen, the printing direction was either parallel or orthogonal to the normal vector of the disks. Then, these disks were subjected to HPT processing using a facility with quasi-constrained configuration [62]. HPT processing was conducted for  $\frac{1}{2}$ , 1, 5 and 10 turns at

**Figure 1** A schematic showing the two orientations of 3D-printing (i.e., the laser beam) lying parallel or orthogonal to the normal of the disks processed subsequently by HPT.



RT under a pressure of 6.0 GPa at a rotational speed of 1 rpm.

### Microstructure characterization

The microstructure of the studied samples was investigated by X-ray diffraction (XRD). In the case of the HPT-processed disks, XRD measurements were taken at both the center and edge parts in order to reveal the effect of plastic strain on the microstructure. The XRD patterns were taken by a diffractometer with  $\text{CoK}_{\alpha 1}$  radiation (wavelength:  $\lambda = 0.1789$  nm). A very narrow and parallel X-ray beam was used, which was monochromatized with a Ge single-crystal monochromator. The beam had a rectangular shape with a dimension of  $0.2 \times 2$  mm<sup>2</sup>. The scattered X-ray radiation was detected by two-dimensional imaging plates. The measurement of a full diffraction pattern took 3 days. The intensity at a given scattering angle ( $2\theta$ ) was obtained by integrating the signal along the corresponding Debye–Scherrer ring. The angle difference between the neighboring measured points was  $0.015^\circ$ . The sample surface before XRD experiments was first mechanically polished with 1200, 2500 and 4000 grit SiC abrasive papers, and then, the polishing was continued with a colloidal silica suspension (OP-S) with a particle size of 40 nm. Finally, the surface was electropolished at 28 V and 0.5 A using an electrolyte with a composition of 70% ethanol, 20% glycerine and 10% perchloric acid (in vol%).

The parameters of the fcc microstructure were determined from the XRD patterns by X-ray line profile analysis (XLPA) using the convolutional multiple whole profile (CMWP) fitting method [71]. During CMWP fitting, the diffraction pattern is fitted by the sum of a background spline and the convolution of the instrumental pattern and the theoretical line profiles related to the parameters of the microstructure, namely crystallite size, dislocations and twin faults. In the HPT-processed samples, the physical broadening of the profiles was much larger than the instrumental broadening, and therefore, instrumental correction was not applied in the evaluation. The theoretical profile functions related to crystallite size, dislocations and twin faults are given in Ref. [68]. The following microstructure parameters obtained by the CMWP fitting are given in this study: the area-weighted mean crystallite size ( $\langle x \rangle_{\text{area}}$ ), the average dislocation density ( $\rho$ ) and the twin fault probability ( $\beta$ ). The latter

quantity corresponds to the fraction of {111} crystallographic planes containing twin faults [72].

The initial AM-prepared samples were also investigated by electron backscatter diffraction (EBSD) using a JEOL-IT700HR-LA Field Emission scanning electron microscope (SEM) equipped with an Oxford Symmetry S3 EBSD detector. The surface treatment before EBSD was the same as for XRD. The applied step size was 0.5  $\mu\text{m}$ , and the EBSD images were evaluated using Oxford AztecCrystal software. The datasets were cleaned by routine wild spike and iterative zero solution process (called Auto Clean in the software). On the inverse pole figures (IPF) maps, only those areas were considered as grains that contain at least 10 pixels and are bounded by high-angle grain boundaries (HAGBs) with a misorientation angle higher than  $15^\circ$ .

### Analysis of chemical composition

The chemical composition of the AM-prepared samples was determined by energy-dispersive X-ray spectroscopy (EDS) using an FEI Quanta 3D scanning electron microscope (SEM). The uncertainty of the constituent element concentrations was  $\pm 0.1$  wt%.

### Hardness testing

The microhardness of the AM-prepared samples and along the diameter of the HPT-processed disks was measured using a Zwick Roell ZH $\mu$  hardness tester with a Vickers indenter. The experiments were performed at RT using an applied load of 500 g and a dwell time of 10 s. The error of the hardness values was estimated from five individual measurements taken on the initial samples and the edge of the disks processed by HPT.

### Experimental results

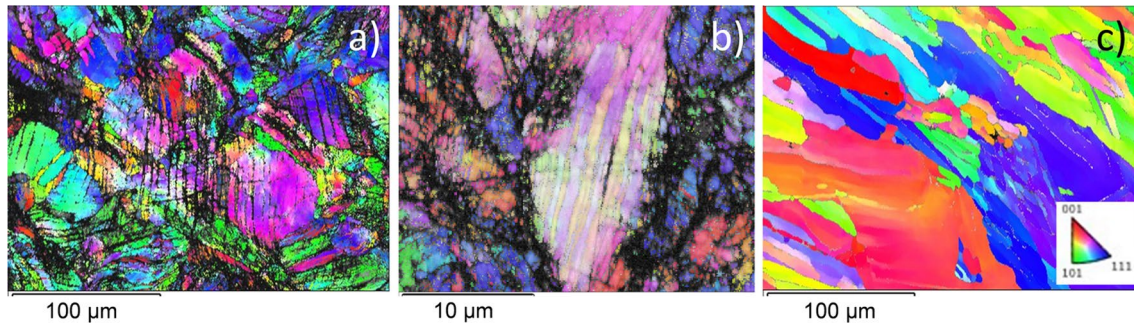
The chemical compositions of the AM-prepared disks printed in parallel and orthogonal directions are shown in Table 1. The main alloying elements are Cr and Ni with concentrations of about 17 and 12 wt%, respectively. Significant compositional difference between the samples printed in parallel and orthogonal directions was not observed.

The inverse pole figure (IPF) maps taken by EBSD on the surfaces of the disks printed in parallel and

**Table 1** The chemical composition of the 316L steel samples processed by AM and casting (in wt%)

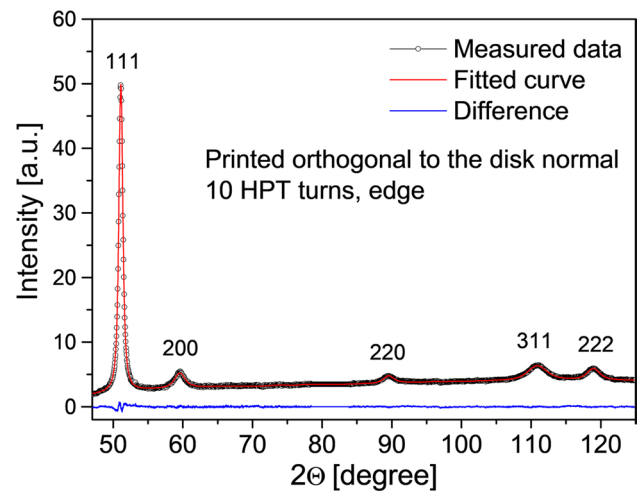
	Fe	Cr	Ni	Si	Mo	Mn	Cu	Co
AM, parallel	65.0	16.9	12.4	0.9	2.5	1.5	0.2	0.6
AM, orthogonal	65.1	17.2	12.3	0.8	2.5	1.3	0.2	0.6
As-cast	69.1	17.2	9.0	0.8	2.1	1.0	0.5	0.3

The terms parallel and orthogonal indicate the relative orientation between the building direction and the normal of the HPT disk. The uncertainty of the concentration values is  $\pm 0.1$  wt%

**Figure 2** IPF maps obtained by EBSD for the initial AM-prepared disks printed parallel (a, b) or orthogonal (c) to the normal direction of the HPT disk.

orthogonal directions are shown in Fig. 2. For the samples AM-prepared in parallel and orthogonal directions, the average grain size values obtained from the IPF images were 4 and 20  $\mu\text{m}$ , respectively. In the IPF map taken on the sample prepared by AM in parallel direction, elongated black areas are visible. In these regions, the determination of the orientation by EBSD was not successful, most probably due to the very small grain size. Therefore, a smaller area was studied again with a much lower EBSD scan step size (0.1  $\mu\text{m}$  instead of 0.5  $\mu\text{m}$ ) in Fig. 2b. Despite the significant refinement of the EBSD scan, some areas remained black, suggesting a nanocrystalline microstructure in these regions. It is worth noting that the grain in the middle of Fig. 2b contains numerous twin boundaries with an average spacing of about 1  $\mu\text{m}$ . In Fig. 2c, the elongated grain shape was caused by the 3D-printing, i.e., the longer axis of the grains is parallel to the printing direction.

Figure 3 shows an XRD pattern taken after 10 turns of HPT at the edge of the disk processed by 3D-printing in the orthogonal direction. The diffractogram reveals that the material has a single-phase fcc structure. A similar observation was made for both the center and edge parts of the studied disks, irrespective of the printing direction and the number of HPT turns, and also for the initial AM-prepared samples. The stability of the fcc phase during SPD,

**Figure 3** X-ray diffractogram obtained at the edge of the disk processed by 3D-printing orthogonal to the disk normal and subsequently by HPT for 10 turns. The experimental pattern is shown by open circles, while the calculated diffractogram fitted to the measured pattern is indicated by a red curve. At the bottom of the figure, the difference between the measured and calculated patterns is shown by a blue curve.

i.e., the lack of martensitic phase transformation from fcc  $\gamma$ -phase to bcc  $\alpha$ -phase, can be attributed to the high (about 12 wt%) Ni content of the present 316L stainless steel (see Table 1). Nickel is a

well-known stabilizer element of the fcc  $\gamma$ -phase [2, 3].

The average crystallite size, the dislocation density and the twin fault probability obtained by XLP A versus the shear strain imposed during HPT are plotted in Fig. 4. The shear strain is determined as [62]:

$$\gamma = \frac{2\pi rN}{t} \quad (1)$$

where  $r$ ,  $N$  and  $t$  are the distance from the disk center, the number of turns and the thickness of the disk, respectively. It should be noted that as the height of the X-ray spot on the studied surface was 2 mm with a negligible width of 0.2 mm, the measurements taken nominally at the center correspond to an  $r$ -value of 0.5 mm, and this value is inserted into Eq. (1). At the periphery, the microstructure was investigated at a distance of 4 mm from the disk center; therefore,  $\gamma$  was also calculated at  $r = 4$  mm using Eq. (1). It should also be noticed that Eq. (1) gives only a nominal shear strain, which may differ from the real plastic strain.

Namely, the stress field of dislocations developed out of the disk center induces dislocation motion in the center [73], thereby resulting in an induced strain in the exact center, even if the nominal strain is zero there according to Eq. (1). In addition, before the starting of the torsional deformation the samples were loaded under 6.0 GPa, resulting in a preliminary compression strain of about 20%.

Figure 4a reveals that the crystallite size was about 180 nm in the initial AM-prepared samples, irrespective of the 3D-printing direction. The crystallite size decreased with increasing shear strain for both printing directions and achieved its minimum value of about 30 nm at a nominal shear strain of 4. Between the shear strain of 4 and 360, no considerable change in the crystallite size was observed. Figure 4b and c shows, respectively, that the dislocation density and the twin fault probability were enhanced with increasing the shear strain during HPT. The dislocation density in both 3D-printed specimens before HPT was  $18 \times 10^{14} \text{ m}^{-2}$ , while the twin fault probability was in

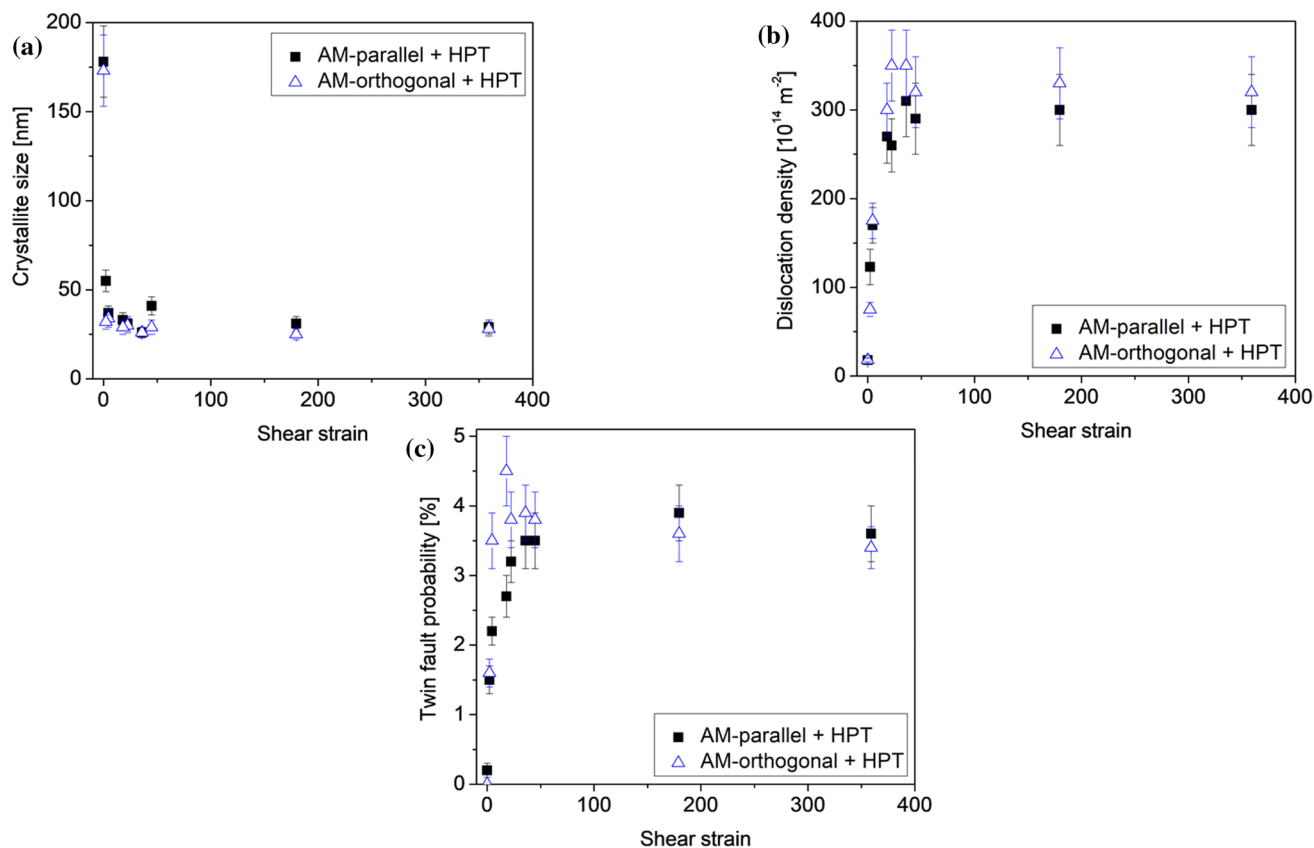


**Figure 4** The crystallite size (a), dislocation density (b) and twin fault probability in the disks printed parallel or orthogonal to the disk normal as a function of the shear strain induced by HPT.

the range of 0–0.2%. The dislocation density got saturated at the value of  $300\text{--}350 \times 10^{14} \text{ m}^{-2}$ , while the maximum achievable twin fault probability was 3.5–4%. For both defects, the saturation occurred at somewhat lower strains for the samples where the laser beam was orthogonal to the disk surface normal as shown in Fig. 4. For instance, the dislocation density saturated at the shear strain of  $\sim 17$  or  $\sim 35$  when the building direction is parallel or orthogonal to the disk normal, respectively. In the case of the twin fault probability, the saturation occurred at the strains of  $\sim 5$  and  $\sim 30$  for “orthogonal” and “parallel” samples, respectively.

The 111, 200 and 220 pole figures obtained by XRD on the samples having surface normal parallel to the building direction are shown in Fig. 5. The pole figures taken for both the initial (AM-prepared) specimen and the disk deformed up to 10 HPT turns are presented in order to reveal the texture change during HPT processing. The AM-prepared sample has a 220 texture, i.e., for most grains, the 220 crystallographic axis is parallel to the normal of the disk. This texture has an almost fiber nature. A schematic in Fig. 6a shows the orientation of the fcc unit cell relative to the disk surface. HPT resulted in a significant change of the texture: after 10 turns the sample has a 111 fiber texture.

In the specimen 3D-printed orthogonal to the disk surface normal, a nearly 220 texture developed during AM-processing as shown in Fig. 7. The inclination angle between the surface normal and the 220 crystallographic direction is about  $10^\circ$  and the orientation distribution is far from a fiber texture unlike in the specimen printed parallel to the disk surface normal. The orientation of the fcc unit cell relative to the disk surface for this sample is shown in Fig. 6b. However, after 10 turns of HPT a 111 fiber texture developed in the “orthogonal” sample similar to the “parallel” specimen. Thus, HPT diminishes the texture difference in the samples 3D-printed in the two directions.

The hardness distribution along the disk diameter for the two samples built in different orientations is shown in Fig. 8 after  $\frac{1}{2}$ , 1, 5 and 10 turns of HPT. The hardness values for the 3D-printed specimens before HPT are also indicated in the graphs. For the AM-prepared samples printed parallel and orthogonal to the disk normal, the hardness values were  $2500 \pm 110 \text{ MPa}$  and  $2340 \pm 70 \text{ MPa}$ , respectively. The very close initial hardness values may be caused by similar microstructural parameters, such as the dislocation density and the grain size. Figure 8 shows that the hardness increased due to HPT for both printing directions but

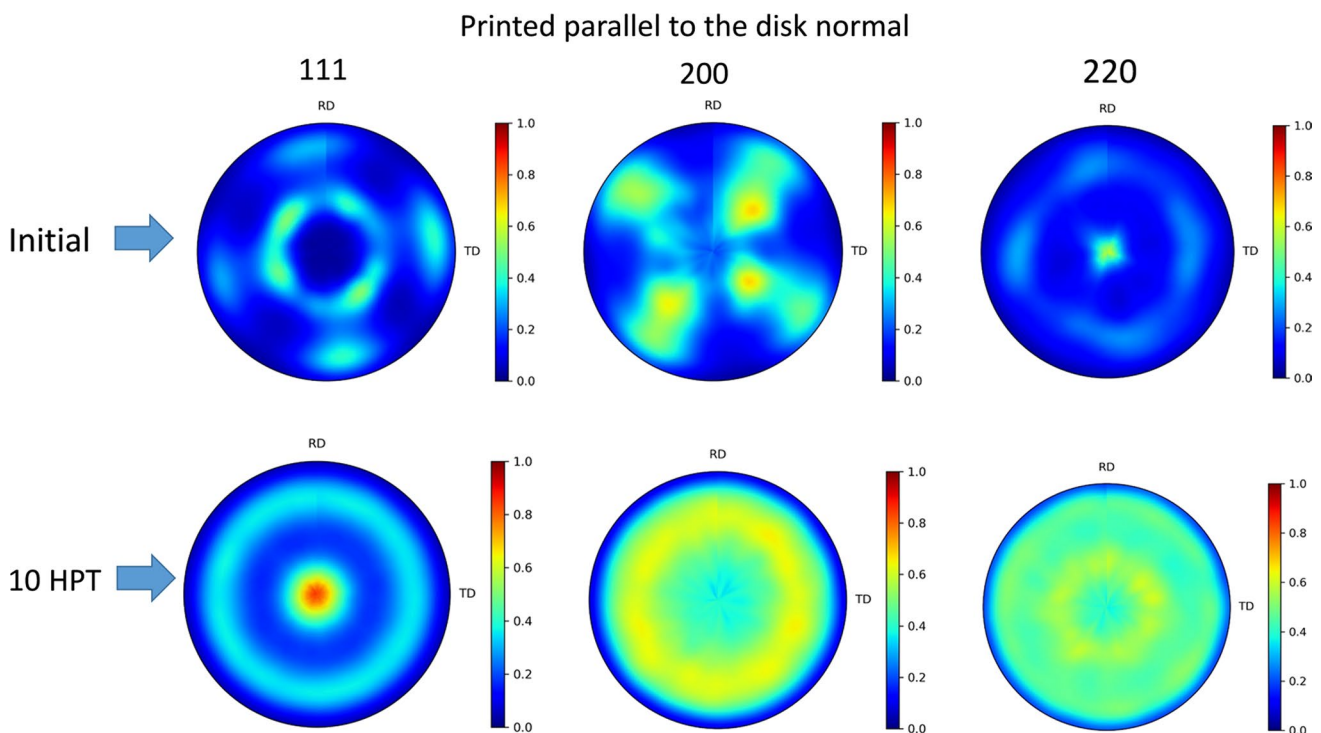


**Figure 5** Pole figures for reflections 111, 200 and 220 obtained for the disk 3D-printed parallel to the disk normal and its counterpart additionally HPT-processed for 10 turns.

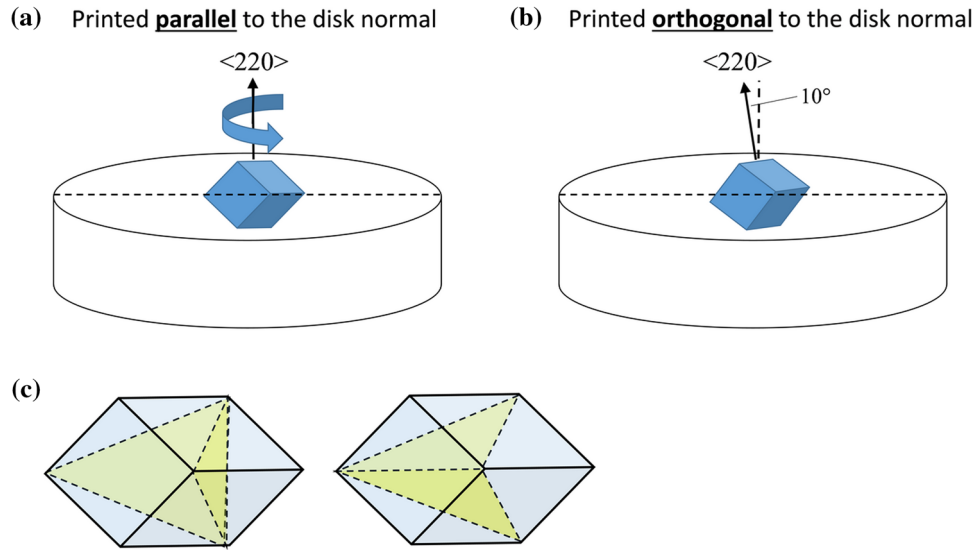


**Figure 6** Schematic showing the orientation of the unit cell of the fcc structure relative to the disk surface for the initial AM-prepared samples printed parallel (a) and orthogonal (b) to the disk normal. The thick curved arrow indicates rotation around the 220 crystallographic axis. Figure c shows the orientation of the four {111} slip planes in the fcc cell presented in (a). In the first

cell, two {111} planes are shown, which are lying perpendicular to the shear stress imposed during HPT; therefore, dislocation glide is not activated on them. In the second cell, the other two {111} slip planes are shown which can serve as glide planes during HPT.

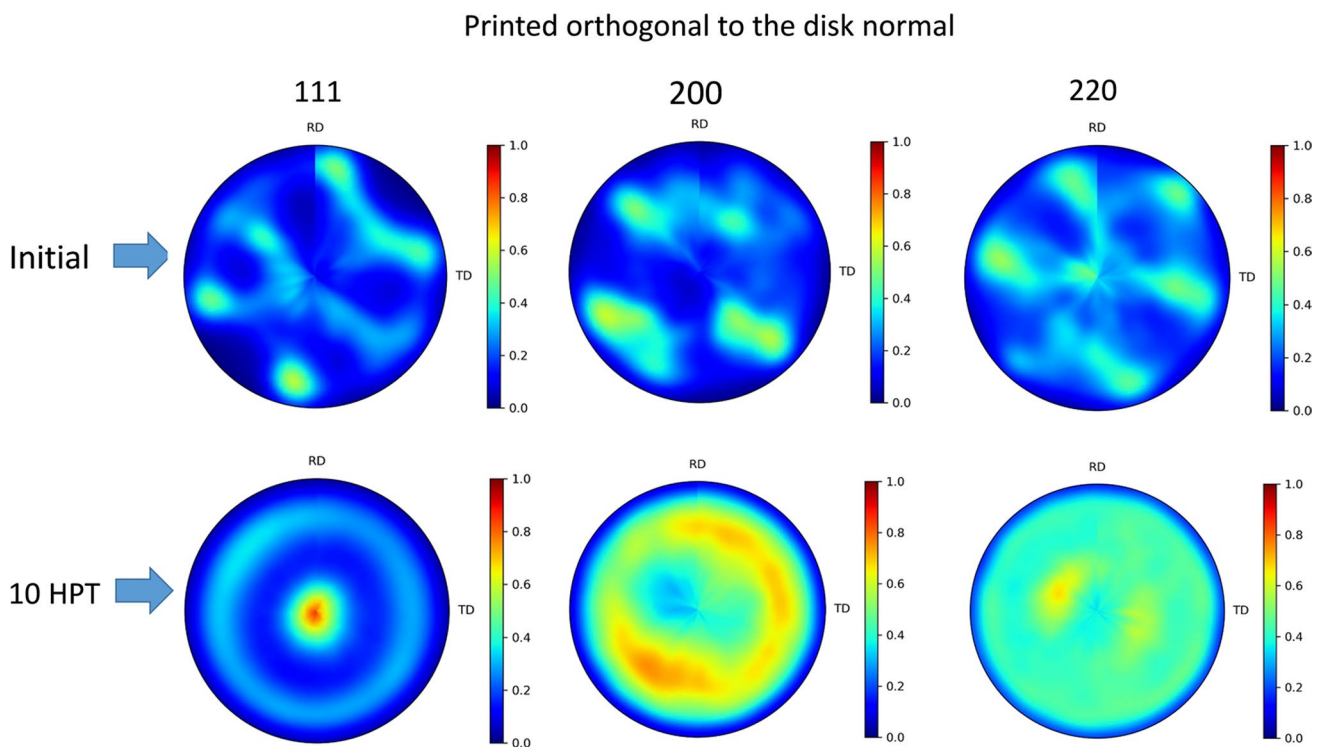


**Figure 7** Pole figures for reflections 111, 200 and 220 obtained for the disk 3D-printed orthogonal to the disk normal and its counterpart additionally HPT-processed for 10 turns.



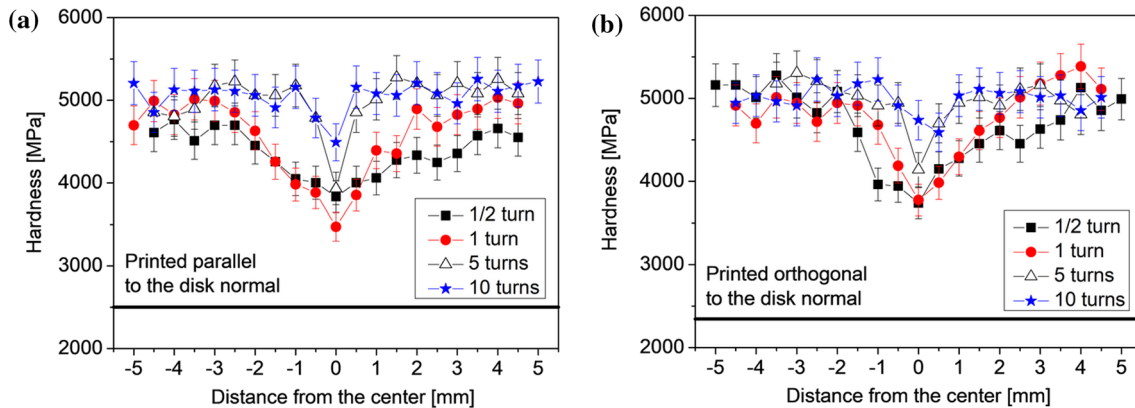


**Figure 8** Hardness versus the distance from the disk center for different numbers of turns obtained on the samples 3D-printed parallel: (a) or orthogonal (b) to the disk normal.

for low numbers of turns (1/2 and 1) the enhancement of the hardness was more pronounced for the printing direction orthogonal to the disk normal. This may be caused by the higher rate of defect density evolution for the latter sample at low shear strains, as revealed in Fig. 4. On the other hand, the saturation hardness was similar for both printing directions with the value of about 5200 MPa, which was observed at the edge part of the disks deformed by 10 turns of HPT.

## Discussion

### Comparison of the microstructure and hardness evolution during HPT in the disks AM-prepared in different directions

In this study, 316L steel disks were processed for HPT by AM applying two different building directions. The hardness of the sample printed parallel to the disk normal exhibited a higher hardness than that for the specimen having a normal vector orthogonal to the building direction (see Fig. 8), which can be attributed to the smaller grain size of the former sample. It should be noted that the grain size obtained by EBSD usually differs from the crystallite size determined by XLPa [68, 71]. Namely, XLPa measures the size of subgrains and dislocation cells in severely deformed metals and alloys since this method is very sensitive to small misorientations (one-tenth of degrees or lower) [68]. Therefore, the crystallite size (or coherently scattering domain size) is usually smaller than the grain

size determined by EBSD as in the latter method the misorientation threshold for grain boundaries is  $15^\circ$ . On the other hand, in the saturation nanocrystalline state achieved by HPT, the crystallite size obtained by XLPa is often very close to the grain size determined by TEM since when the dimension of grains is only tens of nanometers, they have no internal substructure with subgrains or cells [69].

Both as-printed samples contained a significant density of dislocations with the value of about  $18 \times 10^{14} \text{ m}^{-2}$ . A dislocation density with a similar order of magnitude was also detected formerly in a 316L stainless-steel material cast and then deformed by uniaxial tension or compression at RT for the strain of 25% [74]. On the other hand, the origin of dislocations is different in the deformed and the AM-prepared samples. In the former case, the dislocations developed due to plastic deformation while in the latter case dislocations are grown-in defects that formed in order to reduce the mismatch stresses between the misoriented grains nucleated in the laser beam melted layer during building of the AM samples. In addition, the temperature gradient developed in the specimens due to laser heating during AM-processing may cause thermal stresses, which can also yield the formation of dislocations.

At relatively low strains of HPT processing, the defect structure evolution was slightly faster, i.e., the dislocation density and the twin fault probability were somewhat larger for the “orthogonal” sample than in the “parallel” disk. This effect yielded a slightly higher hardness for the former disk at shear strains not higher than  $\sim 30$  as shown in Fig. 9. The difference

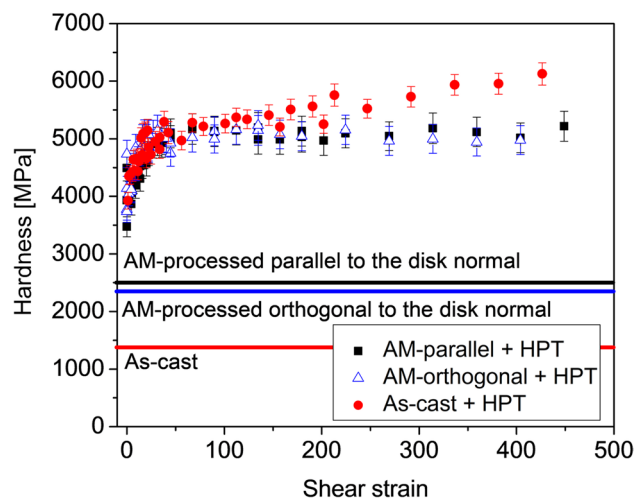


**Figure 9** The hardness as a function of the shear strain imposed during HPT for the disks AM-prepared parallel or orthogonal to the disk normal. For comparison, the hardness versus shear strain is also plotted for the as-cast and HPT-processed 316L steel.

in the dislocation density in the two samples can be attributed to the different crystallographic textures of the as-printed disks. Namely, due to the 220 fiber texture in the “parallel” sample, two {111} planes are perpendicular to the shear stress imposed during HPT (see the left cell in Fig. 6c); therefore, these planes do not serve as glide planes of dislocations at the beginning of HPT processing. On the other hand, the other two {111} planes shown in the right cell in Fig. 6c can be activated by HPT. For the “orthogonal” sample, the 220 crystallographic direction is tilted with about  $10^\circ$  to the HPT disk normal; therefore, dislocation slip systems on all four glide planes can be activated. Thus, the dislocation density increase at the beginning of HPT is somewhat faster for the “orthogonal” sample, compared to the “parallel” disk. With increasing HPT strain, in both sample types a 111 fiber texture formed gradually; thus, the saturation values of the microstructural parameters obtained by XLPAs were consistent for the “orthogonal” and “parallel” disks.

### Comparison of the HPT-induced microstructure evolution in the present AM-prepared samples and formerly studied as-cast 316L steel specimens

In a former study, the same HPT deformation conditions were applied to another 316L stainless steel processed by casting and then annealing at  $1100^\circ\text{C}$  for 1 h [11]. Finally, the samples were quenched to

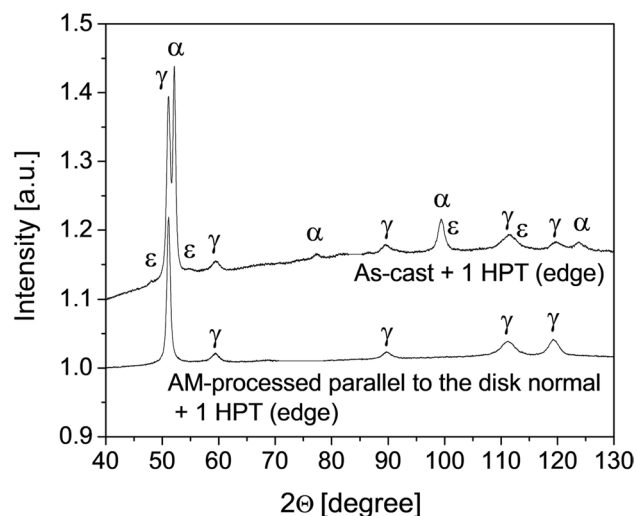


**Figure 10** Comparison of the XRD patterns taken at the edge of the disks processed by 1 turn of HPT from an as-cast and an additively manufactured (AM) 316L material. The 3D-printing was performed parallel to the disk normal.

RT in water to obtain a coarse-grained single-phase  $\gamma$ -austenite microstructure before HPT processing. HPT deformation resulted in a phase transformation first to an hcp  $\epsilon$ -martensite and finally to a bcc  $\alpha$ -martensite with increasing strain. On the other hand, in the present AM-prepared 316L the single-phase austenite microstructure remained stable even up to the shear strain of about 350. As an example, Fig. 10 compares the XRD patterns obtained at the edge of the disks processed by 1 turn of HPT from the as-cast and the AM-prepared 316L material (“parallel” sample). Figure 11 shows the evolution of the phase composition for the as-cast steel as a function of the shear strain imposed during HPT. The fraction of  $\alpha$ -phase increased gradually at the expense of the fcc  $\gamma$ -austenite. Saturation occurred at the shear strain of about 180 when the fractions of the bcc and fcc phases were about 70 and 25%, respectively. The remaining material was an hcp  $\epsilon$ -martensite. The lower stability of the fcc phase in the as-cast material can be attributed to the lower Ni content. Indeed, the AM-prepared and the as-cast samples contained 12 and 9 wt% Ni, respectively. Former investigations have shown that Ni plays an important role in the stabilization of austenite structure in 316L steel [2, 3], which explains the resistance of the AM-prepared samples against phase transformation during HPT.

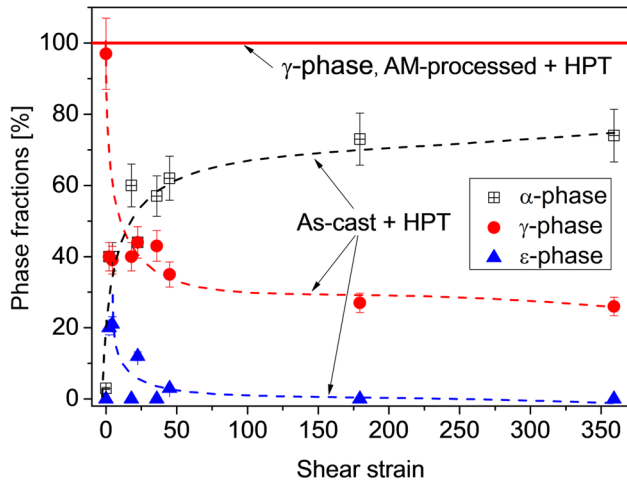


**Figure 11** Evolution of the different phases in the as-cast 316L steel as a function of shear strain imposed during HPT. It is also indicated that in the AM-prepared samples, the whole material remained fully austenite during HPT at least up to the shear strain of about 350.

Figure 12a and b shows the evolution of the parameters of the microstructure versus the shear strain as determined by XLPAs for the  $\alpha$ - and  $\gamma$ -phases in the as-cast 316L material processed by HPT. In the  $\alpha$ -martensite, the crystallite size and the dislocation density first decreased and increased, respectively, with increasing the shear strain and then saturated at the strain of about 50. The minimum crystallite size was 20–25 nm, while the maximum dislocation density was found to be  $\sim 130 \times 10^{14} \text{ m}^{-2}$ . The microstructure was also saturated at the shear strain of about 50 for the  $\gamma$ -phase as shown in Fig. 12b. The minimum crystallite size was similar in both phases, but

the maximum dislocation density was much higher in the fcc phase ( $\sim 250 \times 10^{14} \text{ m}^{-2}$ ). This value is only slightly lower than the saturation dislocation density detected in the AM-prepared 316L samples after HPT ( $300\text{--}350 \times 10^{14} \text{ m}^{-2}$ ). Similarly, the maximum achievable twin fault probability in the  $\gamma$ -phase of the HPT-processed as-cast material ( $\sim 3.5\%$ ) does not differ considerably from the value obtained for the 3D-printed 316L steel deformed by HPT. On the other hand, the saturation of the lattice defect densities occurred at a higher strain (about 50) for the as-cast material compared to the AM-prepared counterparts (between  $\sim 5$  and  $\sim 35$  depending on the printing direction, see Fig. 4). The slower saturation of the microstructure in the fcc phase can be caused by the  $\gamma$ - $\alpha$  phase transformation, which usually occurs at the most severely deformed parts (e.g., at the shear bands) of the HPT-processed stainless steel [11]. Therefore, at low strains, the remaining fcc parts contained a smaller defect density than the 316L counterpart, which did not exhibit phase transformation during HPT (i.e., the 3D-printed samples).

It is worth noting that the saturation dislocation density in the fcc phase of the HPT-processed as-cast 316L steel is about two times higher than that for the coexisting bcc phase. This difference may be caused by the low SFE of the austenite structure (about  $20 \text{ mJ/m}^2$  [75]). The small value of SFE results in highly dissociated dislocations for which the escape from the dislocation pile-ups at glide obstacles is difficult. Therefore, other dislocations must be formed in order to continue plastic deformation in the  $\gamma$ -phase, and thus, a higher maximum dislocation density is achieved than in the  $\alpha$ -phase.

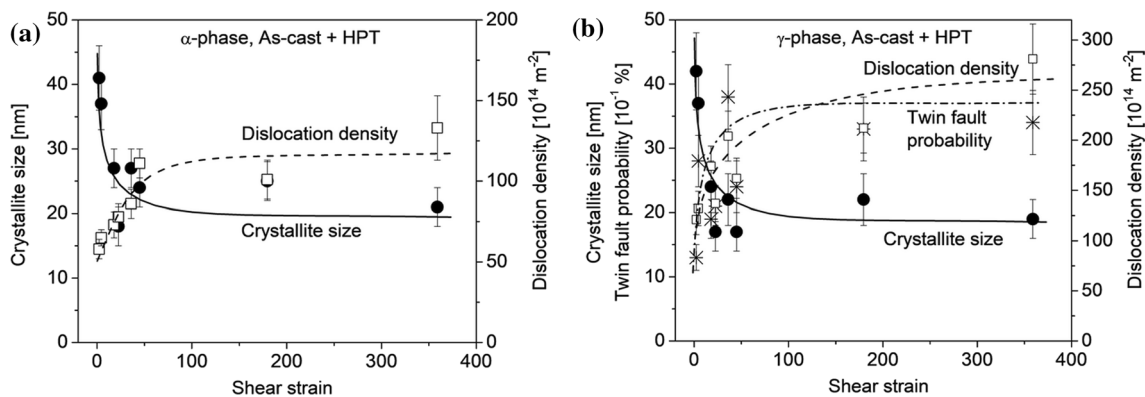


**Figure 12** Evolution of the microstructure parameters in the  $\alpha$ -phase (a) and  $\gamma$ -phase (b) of the as-cast 316L steel versus the shear strain imposed during HPT.

Before HPT, the AM-prepared sample was significantly harder (about 2500 MPa) than the as-cast counterpart (~ 1400 MPa). The much higher hardness of the 3D-printed 316L steel specimens can be attributed to the smaller grain size (4–20  $\mu\text{m}$ ) compared to that of the as-cast material (~ 42  $\mu\text{m}$  [11]). In addition, the AM-prepared samples have a relatively high dislocation density ( $18 \times 10^{14} \text{ m}^{-2}$ ) and the Ni content is also higher than that in the as-cast material. Thus, the dislocation strengthening and the solid solution hardening may also contribute to the elevated hardness of the initial 3D-printed 316L steel. On the other hand, the saturation hardness achieved in the as-cast alloy by HPT was significantly higher than for the HPT-processed AM-prepared samples as shown in Fig. 9. This observation is surprising at first sight since in the saturation state the average dislocation density in the as-cast 316L steel is only about  $160 \times 10^{14} \text{ m}^{-2}$  as calculated from the fractions and the dislocation densities in the  $\gamma$ - and  $\alpha$ -phases, which is half of that for the AM-prepared counterpart. In addition, in the latter material, there is a high amount of twin faults, which also contribute to the hardness. The higher saturation hardness of the HPT-processed as-cast alloy can be explained by the dominance of the  $\alpha$ -phase since the plastic deformation in a bcc structure is usually more difficult than in the fcc counterpart. This effect is due to the reduced mobility of screw dislocations in bcc structures for both glide and cross slip, which is caused by the dissociation of screw dislocation cores into a nonplanar configuration [76]. In fcc crystals, dislocations are split into partials only in their glide planes, which does not hinder their slip and the cross slip of screw dislocations is also easier.

## Conclusions

316L stainless-steel disks were processed by AM and then deformed severely using the HPT technique. The 3D-printing direction was either parallel or orthogonal to the HPT disk normal. The microstructure evolution during HPT was studied by XLP method, and additionally, the hardness was determined as a function of the shear strain. The results of this microstructure study contribute to the understanding of the deformation mechanisms of AM-processed 316L steel at high strains. Moreover, the effect of the building direction on the evolution of the lattice defect structure during HPT is revealed for 316L steel. The significance of

AM-processing in the development of the defect structure during SPD is assessed from the comparison with an as-cast counterpart deformed under the same HPT conditions. The following conclusions were drawn from the experimental results:

- (1) The AM-prepared 316L stainless steel has a single-phase fcc structure irrespective of the printing direction, which remained stable during HPT. The lack of martensitic phase transformation from fcc  $\gamma$ -phase to bcc  $\alpha$ -phase during SPD can be attributed to the high concentration of Ni (about 12 wt%). Both as-printed samples contained a significant density of grown-in dislocations with the value of about  $18 \times 10^{14} \text{ m}^{-2}$ .
- (2) The crystallite size decreased, while the dislocation density and the twin fault probability increased with increasing the shear strain imposed during HPT. The saturation crystallite size, dislocation density and twin fault probability were about 30 nm,  $300\text{--}350 \times 10^{14} \text{ m}^{-2}$  and 3.5–4%, respectively, for both 3D-printing directions. At low strains of HPT processing, the increase of the defect density was slightly higher for the “orthogonal” sample than for the “parallel” disk. This effect can be attributed to the different crystallographic textures of the as-printed disks, yielding a slightly higher hardness for the “orthogonal” disk at shear strains not higher than ~ 30.
- (3) The hardness values of the 316L steel disks printed in different directions varied between 2340 and 2500 MPa, which increased up to about 5200 MPa due to HPT processing. For a formerly studied as-cast 316L steel, the increase of hardness during HPT was higher since a significant martensitic phase transformation occurred due to the lower Ni content (about 9 wt%). The saturation hardness of the HPT-processed as-cast 316L alloy was higher than the 3D-printed counterparts deformed by HPT due to the high fraction of hard bcc martensite (about 70%) even if the fcc AM-prepared samples contained a much higher dislocation density and a large amount of twin faults.

## Acknowledgements

The assistance of Pham Tran Hung in performing X-ray line profile analysis is greatly acknowledged. The authors are grateful to Prof. Heeman Choe for providing the as-cast 316L steel. M. El-Tahawy is grateful to Tempus Public Foundation for providing a short-term study visit to the Eötvös Loránd University, Hungary (AK BE 2020-21 / 157398). Supported by the KDP-2021 Program of the Ministry of Innovation and Technology from the source of the National Research, Development and Innovation Fund.

## Funding

Open access funding provided by Eötvös Loránd University.

## Data availability

Data will be made available on request.

## Declarations

**Conflicts of interest** The authors declare that there is no conflict of interest.

**Ethical approval** Not Applicable.

**Open Access** This article is licensed under a Creative Commons Attribution 4.0 International License, which permits use, sharing, adaptation, distribution and reproduction in any medium or format, as long as you give appropriate credit to the original author(s) and the source, provide a link to the Creative Commons licence, and indicate if changes were made. The images or other third party material in this article are included in the article's Creative Commons licence, unless indicated otherwise in a credit line to the material. If material is not included in the article's Creative Commons licence and your intended use is not permitted by statutory regulation or exceeds the permitted use, you will need to obtain permission directly from the copyright holder. To view a copy of this licence, visit <http://creativecommons.org/licenses/by/4.0/>.

## References

- [1] Kim Y, Kim Y, Kim D, Kim S, Nam W, Choe H (2011) Effects of hydrogen diffusion on the mechanical properties of austenite 316L steel at ambient temperature. *Mater Trans* 52:507–513. <https://doi.org/10.2320/matertrans.M2010273>
- [2] Kang J-H, Noh H-S, Kim K-M, Lee SC, Kim S-J (2017) Modified Ni equivalent for evaluating hydrogen susceptibility of Cr–Ni based austenitic stainless steels. *J Alloys Compd* 696:869–874. <https://doi.org/10.1016/j.jallcom.2016.12.061>
- [3] Odnobokova M, Belyakov A, Enikeev N, Kaibyshev R, Valiev RZ (2020) Microstructural changes and strengthening of austenitic stainless steels during rolling at 473 K. *Metals* 10:1614. <https://doi.org/10.3390/met10121614>
- [4] Eliaz N (2019) Corrosion of metallic biomaterials: a review. *Materials* 12:407. <https://doi.org/10.3390/ma12030407>
- [5] Manivasagam G, Dhinasekaran D, Rajamanickam A (2010) Biomedical implants: corrosion and its prevention—a review. *Recent Pat Mater Sci* 2:40–54. <https://doi.org/10.2174/1877610801002010040>
- [6] Lucas GL, Cooke FW, Friis EA (1999) A primer of biomechanics. Springer, New York
- [7] Baldev R, Kamachi Mudali U, Vijayalakshmi M et al (2013) Development of stainless steels in nuclear industry: with emphasis on sodium cooled fast spectrum reactors history, technology and foresight. *Adv Mater Res* 794:3–25. <https://doi.org/10.4028/www.scientific.net/AMR.794.3>
- [8] Al-Joubori AA, Suryanarayana C (2017) Synthesis of austenitic stainless steel powder alloys by mechanical alloying. *J Mater Sci* 52:11919–11932. <https://doi.org/10.1007/s10853-017-0963-3>
- [9] Wang H, Shuro I, Umemoto M, Ho-Hung K, Todaka Y (2012) Annealing behavior of nano-crystalline austenitic SUS316L produced by HPT. *Mater Sci Eng A* 556:906–910. <https://doi.org/10.1016/j.msea.2012.07.089>
- [10] Mine Y, Horita Z, Murakami Y (2009) Effect of hydrogen on martensite formation in austenitic stainless steels in high-pressure torsion. *Acta Mater* 57:2993–3002. <https://doi.org/10.1016/j.actamat.2009.03.006>
- [11] Gubicza J, El-Tahawy M, Huang Y, Choi H, Choe H, Lábár JL, Langdon TG (2016) Microstructure, phase composition and hardness evolution in 316L stainless steel processed by high-pressure torsion. *Mater Sci Eng A* 657:215–223. <https://doi.org/10.1016/j.msea.2016.01.057>
- [12] Zhong Y, Zheng Z, Li J, Wang C (2021) Fabrication of 316L nuclear nozzles on the main pipeline with large curvature by CMT wire arc additive manufacturing

- and self-developed slicing algorithm. *Mater Sci Eng A* 820:141539. <https://doi.org/10.1016/j.msea.2021.141539>
- [13] DebRoy T, Wei HL, Zuback JS et al (2018) Additive manufacturing of metallic components—process, structure and properties. *Prog Mater Sci* 92:112–224. <https://doi.org/10.1016/j.pmatsci.2017.10.001>
- [14] Haghdadi N, Laleh M, Moyle M, Primig S (2021) Additive manufacturing of steels: a review of achievements and challenges. *J Mater Sci* 56:64–107. <https://doi.org/10.1007/s10853-020-05109-0>
- [15] Hattal A, Mukhtarova K, Djemai M et al (2022) Effect of hot isostatic pressing on microstructure and mechanical properties of Ti6Al4V-zirconia nanocomposites processed by laser-powder bed fusion. *Mater Des* 214:110392. <https://doi.org/10.1016/j.matdes.2022.110392>
- [16] Kawasaki M, Han J-K, Liu X et al (2021) In situ heating neutron and X-ray diffraction analyses for revealing structural evolution during postprinting treatments of additive-manufactured 316L stainless steel. *Adv Eng Mater* 24:2100968. <https://doi.org/10.1002/adem.202100968>
- [17] Morgan R, Sutcliffe CJ, O'Neill W (2004) Density analysis of direct metal laser re-melted 316L stainless steel cubic primitives. *J Mater Sci* 39:1195–1205. <https://doi.org/10.1023/B:JMISC.0000013875.62536.fa>
- [18] Zheng B, Zhou Y, Smugeresky JE, Schoenung JM, Lavernia EJ (2008) Thermal behavior and microstructure evolution during laser deposition with laser-engineered net shaping: Part II. Experimental investigation and discussion. *Metall Trans A* 39:2237–2245. <https://doi.org/10.1007/s11661-008-9566-6>
- [19] Ma M, Wang Z, Wang D, Zeng X (2013) Control of shape and performance for direct laser fabrication of precision large-scale metal parts with 316L Stainless Steel. *Opt Laser Technol* 45:209–216. <https://doi.org/10.1016/j.optlastec.2012.07.002>
- [20] King WE, Barth HD, Castillo VM et al (2014) Observation of keyhole-mode laser melting in laser powder-bed fusion additive manufacturing. *J Mater Process Technol* 214:2915–2925. <https://doi.org/10.1016/j.jmatprotec.2014.06.005>
- [21] Wang X, Deng D, Qi M, Zhang H (2016) Influences of deposition strategies and oblique angle on properties of AISI316L stainless steel oblique thin-walled part by direct laser fabrication. *Opt Laser Technol* 80:138–144. <https://doi.org/10.1016/j.optlastec.2016.01.002>
- [22] Wu AS, Brown DW, Kumar M, Gallegos GF, King WE (2014) An Experimental investigation into additive manufacturing-induced residual stresses in 316L stainless steel. *Metall Mater Trans A* 45:6260–6270. <https://doi.org/10.1007/s11661-014-2549-x>
- [23] Yadroitsev I, Yadroitsava I (2015) Evaluation of residual stress in stainless steel 316L and Ti6Al4V samples produced by selective laser melting. *Virtual Phys Prototyp* 10:67–76. <https://doi.org/10.1080/17452759.2015.1026045>
- [24] Cherry JA, Davies HM, Mehmood S, Lavery NP, Brown SGR, Sienz J (2015) Investigation into the effect of process parameters on microstructural and physical properties of 316L stainless steel parts by selective laser melting. *Int J Adv Manuf Technol* 76:869–879. <https://doi.org/10.1007/s00170-014-6297-2>
- [25] Mertens A, Reginster S, Contrepois Q, Dormal T, Lemaire O, Lecomte-Beckers J (2014) Microstructures and mechanical properties of stainless steel AISI 316L processed by selective laser melting. *Mater Sci Forum* 783–786:898–903. <https://doi.org/10.4028/www.scientific.net/MSF.783-786.898>
- [26] Kamath C, El-dasher B, Gallegos GF, King WE, Sisto A (2014) Density of additively-manufactured, 316L SS parts using laser powder-bed fusion at powers up to 400 W. *Int J Adv Manuf Technol* 74:65–78. <https://doi.org/10.1007/s00170-014-5954-9>
- [27] Yadollahi A, Shamsaei N, Thompson SM, Seely DW (2015) Effects of process time interval and heat treatment on the mechanical and microstructural properties of direct laser deposited 316L stainless steel. *Mater Sci Eng A* 644:171–183. <https://doi.org/10.1016/j.msea.2015.07.056>
- [28] Trelewicz JR, Halada GP, Donaldson OK, Manogharan G (2016) Microstructure and corrosion resistance of laser additively manufactured 316L stainless steel. *JOM* 68:850–859. <https://doi.org/10.1007/s11837-016-1822-4>
- [29] Sun Z, Tan X, Tor SB, Yeong WY (2016) Selective laser melting of stainless steel 316L with low porosity and high build rates. *Mater Des* 104:197–204. <https://doi.org/10.1016/j.matdes.2016.05.035>
- [30] Ma M, Wang Z, Zeng X (2017) A comparison on metallurgical behaviors of 316L stainless steel by selective laser melting and laser cladding deposition. *Mater Sci Eng A* 685:265–273. <https://doi.org/10.1016/j.msea.2016.12.112>
- [31] Godec M, Zaefferer S, Podgornik B, Šinko M, Tchernychova E (2020) Quantitative multiscale correlative microstructure analysis of additive manufacturing of stainless steel 316L processed by selective laser melting. *Mater Charact* 160:110074. <https://doi.org/10.1016/j.matchar.2019.110074>
- [32] Zhang B, Dembinski L, Coddet C (2013) The study of the laser parameters and environment variables effect on mechanical properties of high compact parts elaborated by selective laser melting 316L powder. *Mater Sci Eng A* 584:21–31. <https://doi.org/10.1016/j.msea.2013.06.055>

- [33] Mertens A, Reginster S, Paydas H, Contrepolis Q, Dormal T, Lemaire O, Lecomte-Beckers J (2014) Mechanical properties of alloy Ti–6Al–4V and of stainless steel 316L processed by selective laser melting: influence of out-of-equilibrium microstructures. *Powder Metall* 57:184–189. <https://doi.org/10.1179/1743290114Y.0000000092>
- [34] Riemer A, Leuders S, Thöne M, Richard HA, Tröster T, Niendorf T (2014) On the fatigue crack growth behavior in 316L stainless steel manufactured by selective laser melting. *Eng Fract Mech* 120:15–25. <https://doi.org/10.1016/j.engfracmech.2014.03.008>
- [35] Ziętała M, Durejko T, Polański M et al (2016) The microstructure, mechanical properties and corrosion resistance of 316L stainless steel fabricated using laser engineered net shaping. *Mater Sci Eng A* 677:1–10. <https://doi.org/10.1016/j.msea.2016.09.028>
- [36] Bartolomeu F, Buciumeanu M, Pinto E, Alves N, Carvalho O, Silva FS, Miranda G (2017) 316L stainless steel mechanical and tribological behavior—a comparison between selective laser melting, hot pressing and conventional casting. *Addit Manuf* 16:81–89. <https://doi.org/10.1016/j.addma.2017.05.007>
- [37] Lou X, Othon MA, Rebak RB (2017) Corrosion fatigue crack growth of laser additively-manufactured 316L stainless steel in high temperature water. *Corros Sci* 127:120–130. <https://doi.org/10.1016/j.corsci.2017.08.023>
- [38] Pham MS, Dovgvy B, Hooper PA (2017) Twinning induced plasticity in austenitic stainless steel 316L made by additive manufacturing. *Mater Sci Eng A* 704:102–111. <https://doi.org/10.1016/j.msea.2017.07.082>
- [39] Sun Z, Tan X, Tor SB, Chua CK (2018) Simultaneously enhanced strength and ductility for 3D-printed stainless steel 316L by selective laser melting. *NPG Asia Mater* 10:127–136. <https://doi.org/10.1038/s41427-018-0018-5>
- [40] Li H, Ramezani M, Li M, Ma C, Wang J (2018) Tribological performance of selective laser melted 316L stainless steel. *Tribol Int* 128:121–129. <https://doi.org/10.1016/j.triboint.2018.07.021>
- [41] Shrestha R, Simsiriwong J, Shamsaei N (2019) Fatigue behavior of additive manufactured 316L stainless steel parts: effects of layer orientation and surface roughness. *Addit Manuf* 28:23–38. <https://doi.org/10.1016/j.addma.2019.04.011>
- [42] Kong D, Dong C, Ni X et al (2019) Mechanical properties and corrosion behavior of selective laser melted 316L stainless steel after different heat treatment processes. *J Mater Sci Technol* 35:1499–1507. <https://doi.org/10.1016/j.jmst.2019.03.003>
- [43] Chae H, Huang EW, Jain J et al (2019) Plastic anisotropy and deformation-induced phase transformation of additive manufactured stainless steel. *Mater Sci Eng A* 762:138065. <https://doi.org/10.1016/j.msea.2019.138065>
- [44] Alvi S, Saeidi K, Akhtar F (2020) High temperature tribology and wear of selective laser melted (SLM) 316L stainless steel. *Wear* 448–449:203228. <https://doi.org/10.1016/j.wear.2020.203228>
- [45] Richter J, Bartzsch G, Scherbring S et al (2022) Metastable CrMnNi steels processed by laser powder bed fusion: experimental assessment of elementary mechanisms contributing to microstructure, properties and residual stress. *Sci Rep* 12:21862. <https://doi.org/10.1038/s41598-022-26052-x>
- [46] Dixit S, Liu S, Murdoch HA, Smith PM (2023) Investigating build orientation-induced mechanical anisotropy in additive manufacturing 316L stainless steel. *Mater Sci Eng A* 880:145308. <https://doi.org/10.1016/j.msea.2023.145308>
- [47] Sun Y, Moroz A, Alrbaey K (2014) Sliding wear characteristics and corrosion behaviour of selective laser melted 316L stainless steel. *J Mater Eng Perform* 23:518–526. <https://doi.org/10.1007/s11665-013-0784-8>
- [48] Sander G, Thomas S, Cruz V et al (2017) On the corrosion and metastable pitting characteristics of 316L stainless steel produced by selective laser melting. *J Electrochem Soc* 164:C250. <https://doi.org/10.1149/2.0551706jes>
- [49] Bruycker ED, Sistiaga MLM, Thielemans F, Vanmeensel K (2017) Corrosion testing of a heat treated 316 L functional part produced by selective laser melting. *Mater Sci Appl* 08:223–233. <https://doi.org/10.4236/msa.2017.83015>
- [50] Lou X, Song M, Emigh PW, Othon MA, Andresen PL (2017) On the stress corrosion crack growth behaviour in high temperature water of 316L stainless steel made by laser powder bed fusion additive manufacturing. *Corros Sci* 128:140–153. <https://doi.org/10.1016/j.corsci.2017.09.017>
- [51] Laleh M, Hughes AE, Xu W et al (2019) On the unusual intergranular corrosion resistance of 316L stainless steel additively manufactured by selective laser melting. *Corros Sci* 161:108189. <https://doi.org/10.1016/j.corsci.2019.108189>
- [52] Laleh M, Hughes AE, Xu W, Gibson I, Tan MY (2019) Unexpected erosion-corrosion behaviour of 316L stainless steel produced by selective laser melting. *Corros Sci* 155:67–74. <https://doi.org/10.1016/j.corsci.2019.04.028>
- [53] Kazempour M, Mohammadi M, Mfoumou E, Nasiri AM (2019) Microstructure and corrosion characteristics of selective laser-melted 316L stainless steel: the impact of process-induced porosities. *JOM* 71:3230–3240. <https://doi.org/10.1007/s11837-019-03647-w>
- [54] Man C, Duan Z, Cui Z et al (2019) The effect of sub-grain structure on intergranular corrosion of 316L stainless steel

- fabricated via selective laser melting. *Mater Lett* 243:157–160. <https://doi.org/10.1016/j.matlet.2019.02.047>
- [55] Andreatta F, Lanzutti A, Vaglio E, Totis G, Sortino M, Fedrizzi L (2019) Corrosion behaviour of 316L stainless steel manufactured by selective laser melting. *Mater Corros* 70:1633–1645. <https://doi.org/10.1002/maco.201910792>
- [56] Cruz V, Chao Q, Birbilis N, Fabijanic D, Hodgson PD, Thomas S (2020) Electrochemical studies on the effect of residual stress on the corrosion of 316L manufactured by selective laser melting. *Corros Sci* 164:108314. <https://doi.org/10.1016/j.corsci.2019.108314>
- [57] Kong D, Dong C, Ni X et al (2020) The passivity of selective laser melted 316L stainless steel. *Appl Surf Sci* 504:144495. <https://doi.org/10.1016/j.apsusc.2019.144495>
- [58] Kong D, Dong C, Ni X et al (2020) Superior resistance to hydrogen damage for selective laser melted 316L stainless steel in a proton exchange membrane fuel cell environment. *Corros Sci* 166:108425. <https://doi.org/10.1016/j.corsci.2019.108425>
- [59] Zhou C, Hu S, Shi Q et al (2020) Improvement of corrosion resistance of SS316L manufactured by selective laser melting through subcritical annealing. *Corros Sci* 164:108353. <https://doi.org/10.1016/j.corsci.2019.108353>
- [60] Edalati K, Bachmaier A, Beloshenko VA et al (2022) Nanomaterials by severe plastic deformation: review of historical developments and recent advances. *Mater Res Lett* 10:163–256. <https://doi.org/10.1080/21663831.2022.2029779>
- [61] Valiev RZ, Zhilyaev AP, Langdon TG (2014) Bulk nanostructured materials: fundamentals and applications. John Wiley & Sons, Hoboken, NJ, USA
- [62] Zhilyaev AP, Langdon TG (2008) Using high-pressure torsion for metal processing: fundamentals and applications. *Prog Mater Sci* 53:893–979. <https://doi.org/10.1016/j.pmatsci.2008.03.002>
- [63] Li Z, Ding H, Huang Y, Langdon TG (2022) An evaluation of the mechanical properties, microstructures, and strengthening mechanisms of pure Mg processed by high-pressure torsion at different temperatures. *Adv Eng Mater* 24:2200799. <https://doi.org/10.1002/adem.202200799>
- [64] Figueiredo RB, Cetlin PR, Langdon TG (2011) Using finite element modeling to examine the flow processes in quasi-constrained high-pressure torsion. *Mater Sci Eng A* 528:8198–8204. <https://doi.org/10.1016/j.msea.2011.07.040>
- [65] Gubicza J (2017) Defect structure and properties of nanomaterials. Woodhead Publishing, an imprint of Elsevier, Duxford, UK
- [66] Han J-K, Liu X, Lee I, Kuzminova YO, Evlashin SA, Liss K-D, Kawasaki M (2021) Structural evolution during nanostructuring of additive manufactured 316L stainless steel by high-pressure torsion. *Mater Lett* 302:130364. <https://doi.org/10.1016/j.matlet.2021.130364>
- [67] Csiszár G (2014) Evolution of the Burgers-vector population of Cu–Nb multilayers with 7at% He-implantation determined by X-ray diffraction. *Mater Sci Eng A* 609:185–194. <https://doi.org/10.1016/j.msea.2014.04.110>
- [68] Gubicza J (2014) X-Ray line profile analysis in materials science. IGI global, Hershey, PA, USA
- [69] Gubicza J (2022) Reliability and interpretation of the microstructural parameters determined by X-ray line profile analysis for nanostructured materials. *Eur Phys J Spec Top* 231:4153–4165. <https://doi.org/10.1140/epjs/s11734-022-00572-z>
- [70] Fátay D, Bastarash E, Nyilas K, Dobatkin S, Gubicza J, Ungár T (2022) X-ray diffraction study on the microstructure of an Al–Mg–Sc–Zr alloy deformed by high-pressure torsion. *Int J Mater Res* 94:842–847. <https://doi.org/10.3139/ijmr-2003-0148>
- [71] Ribárik G, Gubicza J, Ungár T (2004) Correlation between strength and microstructure of ball-milled Al–Mg alloys determined by X-ray diffraction. *Mater Sci Eng A* 387–389:343–347. <https://doi.org/10.1016/j.msea.2004.01.089>
- [72] Gubicza J, Chinh NQ, Lábár JL, Hegedűs Z, Xu C, Langdon TG (2008) Microstructure and yield strength of severely deformed silver. *Scripta Mater* 58:775–778. <https://doi.org/10.1016/j.scriptamat.2007.12.028>
- [73] Estrin Y, Molotnikov A, Davies CHI, Lapovok R (2008) Strain gradient plasticity modelling of high-pressure torsion. *J Mech Phys Solids* 56:1186–1202. <https://doi.org/10.1016/j.jmps.2007.10.004>
- [74] El-Tahawy M, Jenei P, Kolonits T, Han G, Park H, Choe H, Gubicza J (2020) Different evolutions of the microstructure, texture, and mechanical performance during tension and compression of 316L stainless steel. *Metall Mater Trans A* 51:3447–3460. <https://doi.org/10.1007/s11661-020-05782-5>
- [75] Schramm RE, Reed RP (1975) Stacking fault energies of seven commercial austenitic stainless steels. *Metall Trans A* 6:1345–1351. <https://doi.org/10.1007/BF02641927>
- [76] Ngan AHW, Wen M (2002) Atomistic simulation of energetics of motion of screw dislocations in bcc Fe at finite temperatures. *Comput Mater Sci* 23:139–145. [https://doi.org/10.1016/S0927-0256\(01\)00224-5](https://doi.org/10.1016/S0927-0256(01)00224-5)

**Publisher's Note** Springer Nature remains neutral with regard to jurisdictional claims in published maps and institutional affiliations.